CrossMark

High-Precision Displacement Sensing of Monolithic Piezoelectric Disk Resonators Using a Single-Electron Transistor

J. Li[1] · **J. T. Santos[2]** · **M. A. Sillanpää[2]**

Abstract A single-electron transistor (SET) can be used as an extremely sensitive charge detector. Mechanical displacements can be converted into charge, and hence, SETs can become sensitive detectors of mechanical oscillations. For studying small-energy oscillations, an important approach to realize the mechanical resonators is to use piezoelectric materials. Besides coupling to traditional electric circuitry, the strain-generated piezoelectric charge allows for measuring ultrasmall oscillations via SET detection. Here, we explore the usage of SETs to detect the shear-mode oscillations of a 6-mm-diameter quartz disk resonator with a resonance frequency around 9 MHz. We measure the mechanical oscillations using either a conventional DC SET, or use the SET as a homodyne or heterodyne mixer, or finally, as a radio-frequency single-electron transistor (RF-SET). The RF-SET readout is shown to be the most sensitive method, allowing us to measure mechanical displacement amplitudes below 10^{-13} m. We conclude that a detection based on a SET offers a potential to reach the sensitivity at the quantum limit of the mechanical vibrations.

1 Introduction

The measurement of atto-Newton forces, or sub-Ångstrom displacements, has a wide range of existing or potential applications, from magnetic resonance force microscopy

---

✉ J. Li
lijian16@nudt.edu.cn

[1] Interdisciplinary Center of Quantum Information, National University of Defense Technology, Changsha 410073, China

[2] Department of Applied Physics, Aalto University, P.O. Box 15100, 00076 Aalto, Finland

[1] to the study of frontiers of physics such as gravitational waves or quantum effects in the motion of mechanical resonators [2–5]. Magnetomotive [6–9], optical interferometric [10,11] as well as mixing [12,13] detection techniques have been widely utilized in fundamental research. Moreover, we mention approaches that are based on the concept of cavity optomechanics, where the mechanical oscillations affect the electromagnetic fields inside either an optical [14–16] or an electrical [17] resonator.

The original detection approaches used in fundamental research included, for instance, the magnetomotive technique that, however, suffers from the need of high fields and bulky equipment. Similarly, optical interferometry also endures the latter issue, and the laser spot size limits the size of the mechanical resonator that can be studied. While impressive quantum experiments have been performed using cavity optomechanics either in optical or in microwave frequency range, the laser or microwave powers that are needed tend to be high and heat up the system. Therefore, one should look for even less intrusive detection techniques that would work at extremely small power. To this end, several experiments have taken advantage of a single-electron transistor (SET) [18,19], which is an ultimate charge-sensitive device and can be capacitively coupled to mechanical devices [20–22]. In such scheme, a DC voltage bias of the order of several volts is applied to a conductive mechanical resonator, and the mechanical vibrations modulate the amount of charge coupled to the SET. In the most delicate measurements, the SET has been replaced by superconducting qubits that bring the system in the quantum regime [23–28].

In our recent work [29], we show how a massive piezoelectric resonator coupled to superconducting microcircuits [30] can be analyzed as a cavity optomechanical device, with implications in studies of quantum-mechanical phenomena. The sensitivity advantage offered by piezoelectric transduction [20,31,32] is highly beneficial for studying and further using the quantum properties of truly macroscopic resonators that can exhibit long-energy lifetimes but nearly vanishing amplitudes of their zero-point motion.

In practical usage, a SET has a very limited bandwidth. The typical large tunnel junction resistance needed for the Coulomb blockade, together with the ever-present stray capacitance from the cables, limits the output bandwidth to about 10^4 Hz. A first stage amplifier in close proximity to the SET [33,34] can extend the bandwidth to $10^6 \ldots 10^7$ Hz at best. There are two standard options to circumvent this limitation and broaden the spectral range of the SET. One is to use it as a radio-frequency (RF) mixer, either in homodyne, or in heterodyne measurement scheme [35,36], taking advantage of the nonlinear dependence of the SET current response to the gate charge. This approach does not increase the instantaneous bandwidth of the SET, which is still limited by the RC charging time, but allows to tune the measurement center frequency up to 10 GHz [35]. The second approach is to use an RF-SET [37], where a series inductance resonates with the cable stray capacitance, creating an LC tank resonator that impedance matches the SET to the low impedance cables, unlocking bandwidth up to 100 MHz [38].

In this article, we investigate a mechanical system that is a 6-millimeter-diameter and 200-microns-thick quartz disk resonator (Fig. 1e) that has the first shear-mode resonance frequency at $\omega_0/2\pi \sim 9$ MHz. A major motivation for studying such monolithic resonators is that they can have exceedingly high mechanical quality fac-
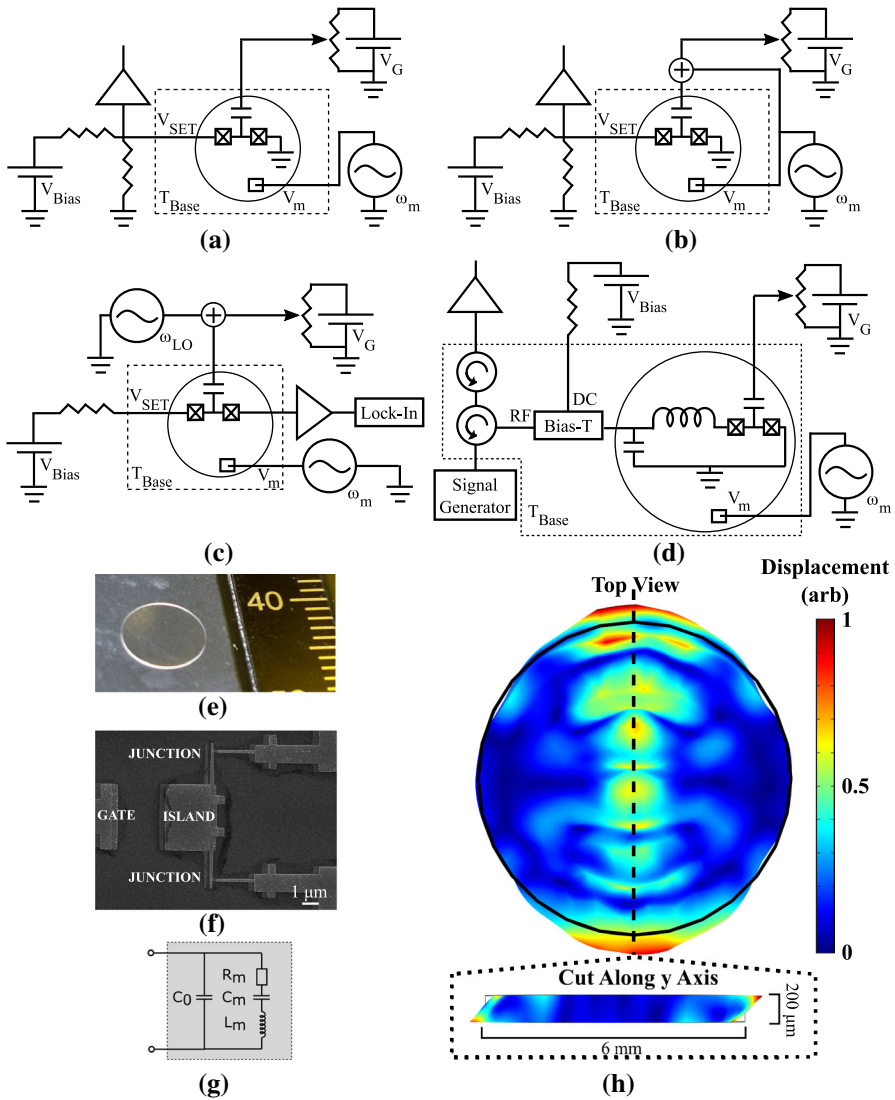
Fig. 1 Measurement scheme for detecting vibrations of the massive quartz disk via SET, using **a** DC rectification; **b** homodyne and **c** heterodyne detection using the SET as a mixer; and **d** RF-SET. The disk represents the quartz resonator/substrate. Drawings not to scale. **e** Photograph of the 6-mm quartz disks used both as the mechanical element and as the substrate where the SET circuit is fabricated. **f** Scanning electron microscope (SEM) image of the SET device with a 3 μm × 4 μm island. **g** Electrical resonant circuit equivalent to a piezoelectric mechanical resonator. **h** Simulated shear-mode shape. The black circle represents the quartz disk edges, and the color codes indicate the deformation. The displacement values are normalized to the maximum displacement. The side view dimensions are not in scale (Color figure online)

tors, paving the way toward macroscopic quantum mechanics [39]. These systems are truly macroscopic with the mode effective mass around 20 mg. We study the prospect of measuring the disk vibrations using four different SET detection setups: DC (Fig. 1a), homodyne mixing (Fig. 1b), heterodyne mixing (Fig. 1c) and RF-SET (Fig. 1d). The

SETs are fabricated directly on top of the quartz disk (Fig. 1f), that acts as both the mechanical element and the substrate for the fabrication of the electrical circuit. The basic idea is independent of the measurement scheme chosen: the deformation of the quartz disk generates piezoelectric charge on the chip surface; the charge created in the vicinity of the SET island couples to it, thereby modulating the tunneling current or the SET resistance.

2 Piezoelectric Resonator and SET

A piezoelectric resonator can be represented by an equivalent series RLC circuit like the one in Fig. 1g. Let us consider a circular quartz disk with the surface area A, thickness z, shear-mode stress coefficient e_s, shear modulus Y_s, relative permittivity ϵ_r and piezoelectric coupling coefficient $K_0^2 = e_s^2/(\epsilon_0 \epsilon_r Y_s)$. The geometric capacitance in the plate-capacitor approximation is $C_0 = \epsilon_0 \epsilon_r A/z$, and the other equivalent circuit parameters can be calculated as $C_m = K_0^2 C_0$, $L_m = [(2\pi\omega_0)^2 C_m]^{-1}$ and $R_m = (C_m \omega_0 Q)^{-1}$, where Q is the mechanical quality factor. In Table 1, we summarize the quantities mentioned above.

A static shear deformation Δx_0 corresponding to an applied potential difference V between the two faces of the quartz disk is given as

$$\Delta x_0 = \frac{\epsilon_r \epsilon_0}{e_s} V , \qquad (1)$$

that amounts to less than a nanometer displacement per volt. In a dynamical situation, close to the mechanical resonance, the resonator amplifies the applied voltage V_m with the frequency ω_m, cf. the equivalent electrical circuit in Fig. 1g, and one obtains the

Table 1 Geometric and material parameters of the quartz disk resonator and an approximation of the correspondent equivalent electrical quantities when modeling the mechanical resonator as the RLC circuit of Fig. 1g

Parameter	Symbol	Value	Unit
Disk surface area	A	2.8×10^{-5}	m^2
Disk thickness	z	2×10^{-4}	m
Quartz shear modulus	Y_s	3×10^{10}	Pa
Quartz shear stress coefficient	e_s	1×10^{-1}	$C\,m^{-2}$
Quartz relative permittivity	ϵ_r	4.5	
Disk mechanical frequency	ω_0	$2\pi \times 9$	MHz
Coupling coefficient	$K_0^2 = e_s^2/(\epsilon_0 \epsilon_r Y_s)$	8×10^{-3}	$m^2 C^{-1}$
Geometric capacitance	$C_0 = \epsilon_0 \epsilon_r A/z$	5×10^{-12}	F
Mechanical capacitance	$C_m = K_0^2 C_0$	4×10^{-14}	F
Mechanical inductance	$L_m = [\omega_m^2 C_m]^{-1}$	8×10^{-3}	H
Mechanical resistance	$R_m = (C_m \omega_m Q)^{-1}$	30	Ω
Mechanical quality factor	Q	15×10^3	

dynamical vibration amplitude

$$\Delta x = \frac{e_s V_m}{\gamma Y_s z} \frac{\sinh(\gamma z/2)}{\cosh(\gamma z/2)} , \tag{2}$$

where

$$\gamma^2 = -\frac{\omega_m^2/v_0^2}{1 + i/Q} , \tag{3}$$

and $v_0 \approx 3540 \ \mathrm{ms}^{-1}$ is the sound speed of shear waves in quartz.

In the experiment, we actuate the vibrations through a separate excitation electrode shown in Fig. 1a–d. Equation (2) holds only for the part of the chip covered by the excitation electrode, while we are interested in the amplitude under the SET island somewhat distant from the electrode. In order to enable experimental comparison, we need to know how much the amplitude is reduced from that in Eq. (2) due to the small overlap. To this end, we run a COMSOL simulation and compare a full electrode coverage versus the actual chip layout, obtaining a reduction factor $\beta \simeq 0.11$ that should multiply the right-hand side of Eq. (2).

Assuming a uniform piezoelectric charge distribution across the disk surface, a shear deformation Δx corresponds to a shear strain $\lambda_s = \Delta x/z$ and generates a piezoelectric surface charge density $\sigma_q = \lambda_s e_s$. Then, the number of electron charges coupled to a SET island is

$$n_{\mathrm{isl}} \approx \sigma_q A_{\mathrm{isl}} = \frac{\Delta x e_s A_{\mathrm{isl}}}{ze} . \tag{4}$$

Here, A_{isl} is the effective quartz surface area over which the SET sees the piezo-charge. It is of the order the SET island area, but larger by a small numerical factor.

We model the SET response to charge as follows: If there is a total charge n_g coupled to the SET island, we suppose the periodic gate charge response of the SET can be approximated as sinusoidal:

$$I_{\mathrm{SET}} = i_0 - \frac{I_0}{2} \cos\left(\pi n_g\right) , \tag{5}$$

which represents the $2e$ periodicity of a superconducting SET. Here, I_0 is the peak-to-peak amplitude of gate modulation, and i_0 the average current, both of which depend on the SET bias. The nonlinearity of the SET is the basis for the DC and mixing detection methods. The most general case of gate charge setting discussed below consists of three terms. There is usually a nonzero constant offset n_{g0}, and around the offset the gate charge is supposed to oscillate sinusoidally in time due to the mechanical oscillations driven at the frequency ω_m. Moreover, in the mixing schemes, there is a strong local oscillator at the frequency ω_{LO} and with the amplitude n_{LO}:

$$n_g(t) = n_{g0} + n_{\mathrm{isl}} \cos\left(\omega_m t\right) + n_{\mathrm{LO}} \cos\left(\omega_{\mathrm{LO}} t\right) . \tag{6}$$

The nested sinusoidal behavior of Eqs. (5, 6) will be seen in the experimental data below.

3 Results

In the measurements, we used two individual samples, labeled A and B. Sample A was used in all the other measurements except in the heterodyne scheme (Fig. 1c). The samples were essentially similar, but sample B had a smaller junction resistance, although this plays only a minor quantitative role in the results.

We begin with discussing the current–voltage (IV) properties of the SET in sample A. It comprises a 3 μm $\times$ 4 μm island delimited by two Al (30 nm)/AlOx/Al (60 nm) tunnel junctions made by shadow evaporation. For the measurements, the edges of the chip with the SET are firmly glued to a sample stage, but the center of the chip is free to vibrate. All the measurements discussed in this paper were taken in a dilution refrigerator at a temperature of $\sim$ 20 mK. The sum resistance of the two junctions of our SET in sample A is approximately 169 kΩ, and the charging energy is estimated as 0.3 K.

The standard DC IV measurement involves the biasing scheme shown to the left in Fig. 1a–c. We apply current bias through a 8.8 MΩ resistor for the schemes in Fig. 1a, b and through 100 kΩ in Fig. 1c. Figure 2a shows the DC IV properties for our SET device. The width of the I_{SET} current plateau is mostly set by the superconductor gap in our superconducting device. The Coulomb blockade modulation as a function of the gate voltage V_G is visible at edges of the plateau.

In the quartz vibration measurements with sample A, we use the optimal $V_{SET} \approx$ 0.86 mV biasing point around the gap edge, which maximizes the modulation of I_{SET} by V_G, marked by an arrow in Fig. 2a. Figure 2c displays the gate dependence of the current around such optimal biasing, showing approximately sinusoidal dependence with a peak-to-peak amplitude of $I_0 \approx$ 0.9 nA. Here and throughout the paper, we refer to the gate voltage as the value at the room-temperature generator, preceding the cryogenic voltage division.

3.1 DC Readout with the SET

We begin with a simple rectification approach where $n_{LO} = 0$ in Eq. (6), allowing to measure large-amplitude vibrations. Equation (5) becomes
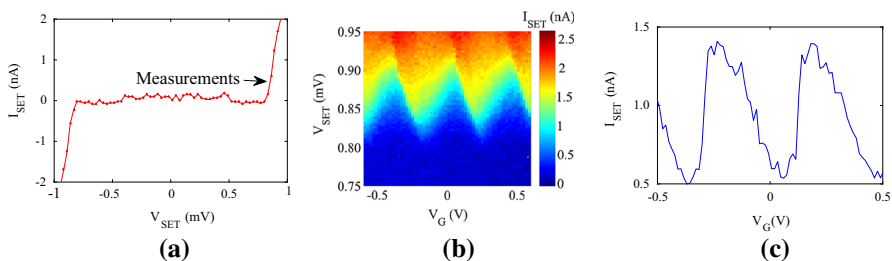

Fig. 2 **a** Sample A: DC IV curve for the SET measured with the setup of Fig. 1a when the gate voltage $V_G = 0$. **b** Dependence of the current through the SET on V_G for the bias values around the steepest part of the IV curve presented in this figure **a**. **c** Dependence of the SET current on gate voltage for an optimal V_{SET} biasing of 0.86 mV (Color figure online)

$$I_{SET} = i_0 - \frac{I_0}{2} \cos\left(\pi n_{g0}\right) J_0\left(\pi n_{isl}\right) , \tag{7}$$

where J_0 is the zeroth-order Bessel function of the first kind.

Now we excite the mechanical vibrations with voltage, thereby creating nonzero n_{isl}. Physically, the piezoelectric charge modulates the SET current by changing the potential of the island, in the same way as the gate voltage. In Fig. 3a, we display such a measurement for different values of V_G. The mechanical resonance can be observed at $f_0 = 8.865$ MHz, as a sharp feature that depends on the gate bias. Looking at Eq. (7), the data qualitatively match the prediction. At the current minima or maxima, where $\cos\left(\pi n_{g0}\right) = 1$, the peak is roughly the maximum in amplitude, but disappears at the intermediate values when $\cos\left(\pi n_{g0}\right) \approx 0$. Also, the sign of the peak changes according to the prediction.

In Fig. 3b, we display an example of a resonance peak measured at a rather large mechanical excitation voltage of 13 mV$_{RMS}$, corresponding to a displacement around 27×10^{-12} m calculated from Eq. (2). At higher mechanical excitation amplitudes, the SET current, however, starts to decrease as shown in Fig. 3c at $V_m \approx 10$ mV$_{RMS}$ where the driven charge covers more than one gate period. We can make an independent estimate of the crossover voltage by the fact that it corresponds to the first minimum of $J_0\left(\pi n_{isl}\right)$, at $n_{isl} \approx 1.2\ e$, and using Eqs. (2, 4) yielding $V_m \approx 11$ mV, in a good agreement with the measurement.

The lowest mechanical excitation amplitude with which we could still use the DC rectification method to discern the mechanical resonance peak with this setup is $V_m \approx 1.6$ mV$_{RMS}$ that corresponds to $\Delta x \approx 3.4 \times 10^{-12}$ m and $n_{isl} \approx 0.18\ e$. The linewidth of the mechanical peak is ~ 600 Hz, corresponding to a mechanical Q value of $\sim 15 \times 10^3$. That Q value is modest compared to what is in principle achievable with quartz resonators [39]. We expect this is due to the fact that the disk was fully flat in cross-section profile, which does not result in confinement of the mechanical vibration in the disk center, and hence, there can be pronounced energy leakage through the supports.
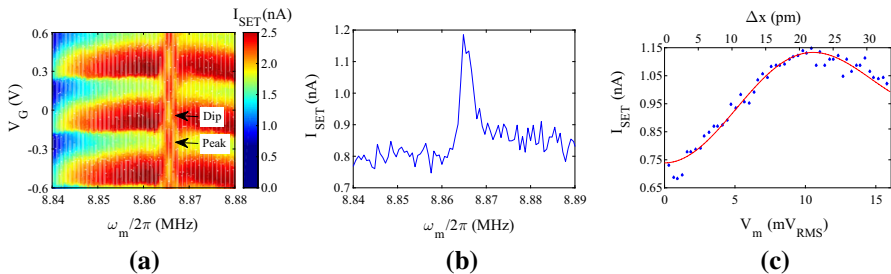

(a)   **(b)**   **(c)**

Fig. 3 Response of the DC measurement SET setup of Fig. 1a (sample A), biased with $V_{SET} = 0.86$ mV, to the driven motion in the piezoelectric quartz disk resonator: **a** gate voltage modulation of the SET current I_{SET} around the mechanical mode frequency at ≈ 8.865 MHz when $V_m \approx 11$ mV$_{RMS}$; **b** the mechanical resonance peak for an actuation voltage $V_m \approx 13$ mV$_{RMS}$, when $V_G \simeq 0.12$ V; **c** the SET current when the mechanical resonator is excited on-resonance at increasing excitation voltages. The solid line is a theoretical curve based on Eqs. (2, 4, 7) with $n_{g0} = 0.31$ and an island interaction area $A_{isl} \approx 18\ (\mu m)^2$ (Color figure online)

3.2 Homodyne and Heterodyne Mixing Schemes

Although the DC rectification is a simple and robust method to obtain the signal at large excitation amplitudes, its sensitivity vanishes toward small vibrations. An improved approach is to use the SET as an RF mixer [35] in the setups shown in Fig. 1b, c. Mixer operation entails that a strong local oscillator (LO) at the frequency ω_{LO}, see Eq. (6), is applied to the SET gate, while the actuation tone goes to the actuation electrode as above. In homodyne detection, the LO frequency is the same as the mechanical excitation frequency, $\omega_{LO} = \omega_m$, and the signal appears as a DC offset similar to the rectification setup. The device has the same bandwidth as the standard SET, but with a tunable measurement center frequency. The DC biasing is done in a fashion similar to that described in the previous section. In terms of complexity, the homodyne setup is comparable to the rectification setup. Analogous to Eq. (7), we obtain the homodyne current

$$I_{DC} \simeq i_0 - \frac{I_0}{2} \cos\left(\pi n_{g0}\right) \left[J_0(\pi n_{LO}) J_0(\pi n_{isl}) + 2 J_1(\pi n_{LO}) J_1(\pi n_{isl}) \right], \qquad (8)$$

which allows for linear detection at small amplitudes. Here, J_1 is the first-order Bessel function of the first kind. In Fig. 4a, we see, similar to Fig. 3a, the mechanical mode at $f_0 \approx 8.865$ MHz. In Fig. 4b, we show the SET current caused by the increase in the mechanical vibration amplitude when the mechanics is actuated on-resonance. The increased sensitivity of the homodyne detection over the DC method enables the visibility of the mechanical resonance peak at smaller mechanical excitation voltages down to $V_0 \approx 0.6$ mV$_{RMS}$. That corresponds to $\Delta x \approx 1.3 \times 10^{-12}$ m and $n_{isl} \approx 0.07\,e$. The theoretical curve plotted in Fig. 4b, calculated from Eq. (8) matches well the homodyne experimental data.
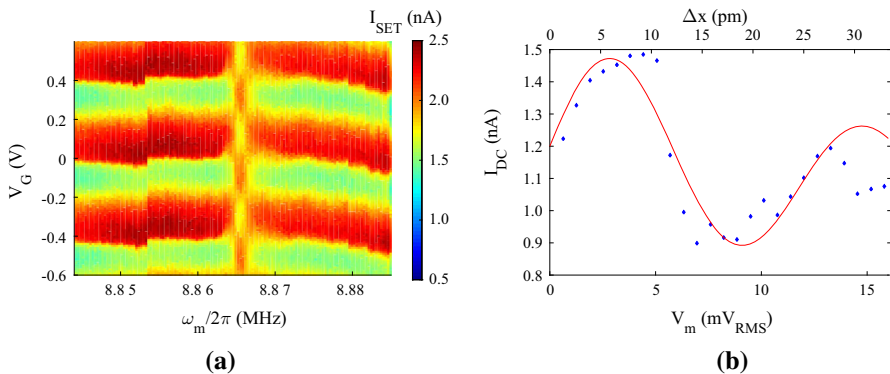

Fig. 4 Quartz disk vibrations detected using the homodyne detection scheme in Fig. 1b (sample A, with the SET biased as shown in Fig. 2a): **a** the SET current as a function of gate voltage and actuation frequency when $V_m = 2.6$ mV; **b** SET drain-to-source current when the mechanical resonator is excited at its resonance frequency $f_0 = 8.865$ MHz with different excitation amplitudes. The device is biased with $V_G = 0.3$ V. The solid line is a theoretical curve based on Eqs. (2, 4, 8) with the same parameters used in Fig. 3c except $n_{g0} = 1$ and $n_{LO} = 0.65$ (Color figure online)
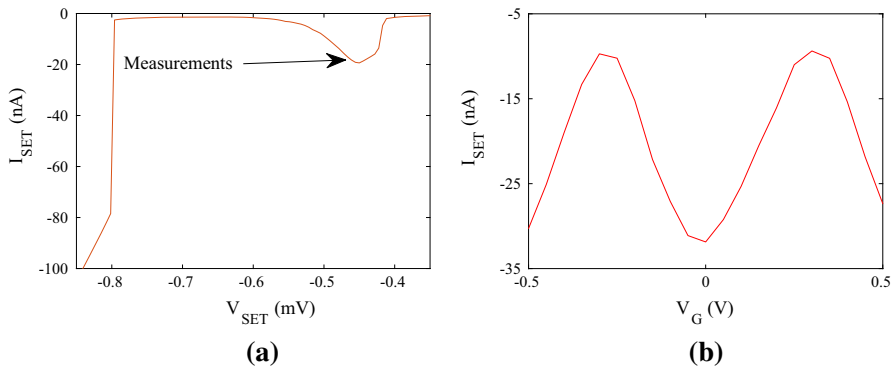
(a)   **(b)**

Fig. 5 **a** Sample B: DC IV curve for the SET measured with the setup of Fig. 1c when the gate voltage $V_G = 0$. **b** Dependence of the current through the SET on V_G for the bias values around the JQP peak (Color figure online)

Direct conversion to DC, either using the DC method or using homodyne detection, encompasses challenges, namely DC offsets from self-mixing of the excitation signal, and in particular, $1/f$ charge noise that is dominant in charge-sensitive devices at low frequencies. In heterodyne detection, the gate electrode is excited by a local oscillator with frequency ω_{LO} different from the mechanical excitation frequency ω_m. The response of the SET current is then mixed down to an intermediate frequency (IF) equal to $\omega_{IF} = \omega_m - \omega_{LO}$. The relevant current is given as

$$I_{IF} = I_0 \cos\left(\pi n_{g0}\right) J_1\left(\pi n_{LO}\right) J_1\left(\pi n_{isl}\right) \cos\left[(\omega_m - \omega_{LO})t\right] . \qquad (9)$$

The intermediate frequency needs to be within the bandwidth of the SET setup. Here, we used $\omega_{IF}/2\pi = 18$ kHz. In the heterodyne setup shown in Fig. 1c, the SET current is detected by a current preamplifier, then acquired by a DAQ board and processed in the frequency domain. Here, we used a different sample B, although the setup is expected to work also with the sample A used for the other measurements discussed. Figure 5a shows the IV curve of the SET in sample B. We operate at the Josephson Quasiparticle (JQP) peak, originated from the tunneling of Cooper pairs through one junction followed by two successive quasiparticle tunneling events through the other junction. Instead of the quasiparticle current onset (Fig. 2a) used in the measurements discussed above, in this sample we found the JQP peak biasing provides a strong gate modulation as shown in Fig. 5b. We relate this to the lower resistance of sample B, providing pronounced Cooper pair tunneling features.

Figure 6a displays the detected mechanical signal, with the local oscillator amplitude roughly optimized. Comparing to Fig. 4a, it is clear that the heterodyne scheme disposes of the DC response of the SET, hence making the data easier to interpret. Figure 6b shows the mechanical resonance peaks for different mechanical excitation amplitudes. The elimination of low-frequency noise by the heterodyne setup allows to measure the mechanical vibrations down to $\Delta x \approx 6 \times 10^{-13}$ m. This is an improvement over the homodyne setup, although since the data were obtained from different samples, the origin of the improvement is not necessarily in the mixing scheme used. The
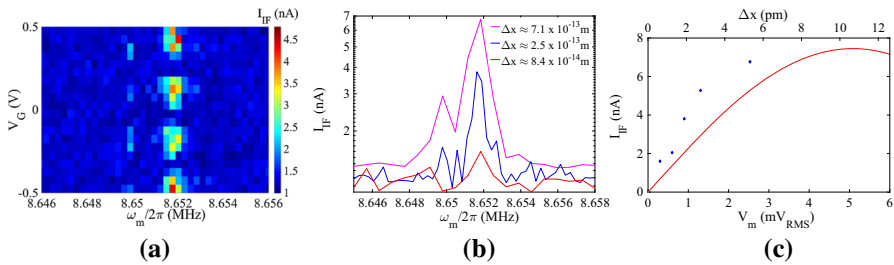
Fig. 6 Response in the heterodyne scheme of Fig. 1c (sample B) with the SET bias $V_{SET} \approx -0.45$ mV: **a** intermediate-frequency SET current as a function of gate bias and mechanical excitation frequency. The mechanical mode is excited with $V_m \approx 0.9$ mV$_{RMS}$ and visible at ≈ 8.652 MHz; **b** resonance peaks acquired at different mechanical excitation amplitudes; **c** response when the mechanical resonator is excited on-resonance. The solid line is a theoretical curve based on Eqs. (2, 4, 9) (Color figure online)

dependence of I_{IF} with the mechanical excitation amplitude is presented in Fig. 6c. The solid line represents a theory curve calculated from Eq. (9) with $I_0 = 22$ nA obtained from Fig. 5b and $n_{LO} = 0.59$. The data points follow the shape of the theoretical curve, however, display double the amplitude as predicted by independent estimates, a fact we attribute to inaccuracies in the local oscillator amplitude.

3.3 Radio-Frequency SET as a Displacement Sensor

In the RF-SET setup [37,40], the SET is impedance-matched to 50 Ω microwave cables via an LC tank resonator circuit. The inductor and capacitor at the input of the SET, see Fig. 1d, form the tank circuit with resonance frequency $\omega_{LC} = (LC)^{-\frac{1}{2}}$, loaded by the SET.

When the SET resistance changes, due to piezo-vibrations as here, the loading of the LC circuit by the SET changes, hence modulating the reflected power of a monochromatic carrier wave sent down the input line. The carrier appears as a time-dependent voltage across the SET, with the amplitude δV. The SET conductance is

$$G_{SET} = \frac{I_{SET}}{V_{SET}} = \frac{i_0 - \frac{I_0}{2}\cos\left(\pi(n_{g0} + n_{isl}\cos\omega_m t)\right)}{V_{bias} + \delta V \cos\omega_{LC} t} . \tag{10}$$

The information is the power of the sidebands that appear at frequencies offset by the actuation frequency from a carrier applied at ω_{LC}, obtained by detecting the carrier at room temperature. Under $\delta V \ll V$, the first sideband amplitude is

$$I_1 = \delta V \frac{I_0}{2} \left|\sin(\pi n_{g0})J_1(\pi n_{isl})\right| . \tag{11}$$

The transmitted and reflected waves are separated by circulators at base temperature stage of the refrigerator, so the reflected power can be measured by a spectrum analyzer. The bias-T allows for DC biasing the SET, needed to obtain a charge-sensitive response.
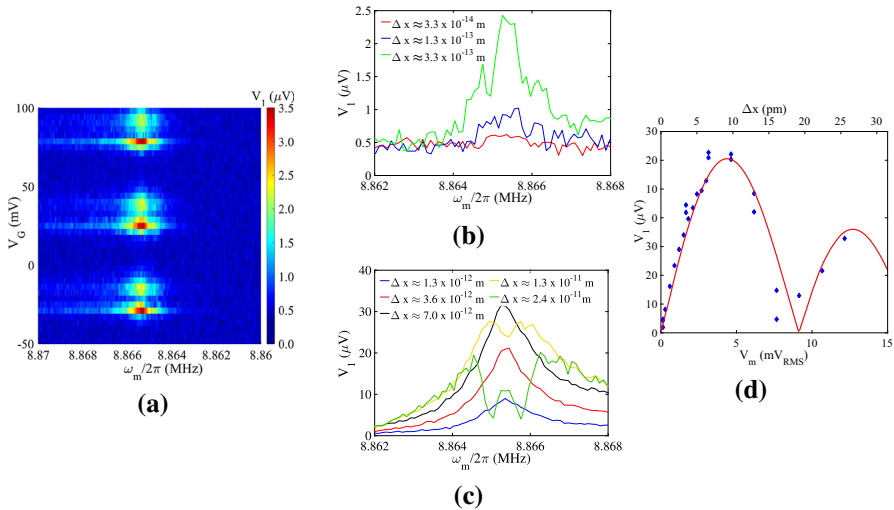
Fig. 7 Measurement of the quartz disk vibrations using the RF-SET scheme of Fig. 1d (sample A) biased with $V_{bias} \approx -0.18$ mV: **a** gate bias dependence of the sideband response whose amplitude is called V_1 in this plot; **b** mechanical resonance peaks measured at various low amplitude mechanical excitation voltages, and $V_G \approx 40$ mV; **c** as (**b**), but high amplitudes; **d** response as a function of excitation amplitude with resonant excitation. The solid line is the theory curve from Eqs. (2, 4, 11), with a carrier amplitude of -86 dBm and an output amplification of 80 dB (Color figure online)

In the present system, the tank circuit capacitance and inductance come from the bonding wires' and bonding pad's stray inductance and capacitance, respectively. The sample box configuration and bonding wires' lengths and placements were simulated with Sonnet software and tweaked to set the tank circuit resonance frequency around 4 GHz to 5 GHz. As an example, Fig. 7a shows a RF-SET measurement displaying the mechanical peak. For the following measurements, the gate and SET bias voltages were chosen so that the maximum SET differential resistance modulation is obtained.

Figure 7b, c presents examples of the mechanical resonance curves. Each curve represents the amplitude of the sideband of the carrier. Similar to the other detection methods discussed above, we can enter the nonlinear regime of the SET response, that is, observe the full Bessel dependence in Eq. (11). Splitting of the peaks is due to the fact that the driven charge n_{isl} at on-resonance drive is larger than at off-resonant drive. The lowest mechanical excitation amplitude with which we could still discern the mechanical resonance peak with this setup is $V_m \approx 15\,\mu V_{RMS}$, which corresponds to $\Delta x \approx 3 \times 10^{-14}$ m, more than 20 times better than the other techniques.

4 Conclusions

We have shown that single-electron transistor (SET) is a viable tool to detect minuscule mechanical vibrations in millimeter-sized monolithic quartz disk resonators. We compared four detection schemes: DC rectification, homodyne and heterodyne mixing

detection, and an approach based on the radio-frequency SET. We found that over the compared schemes, RF-SET is superior in sensitivity over mixing methods, allowing to measure oscillations down to $\sim 3 \times 10^{-14}$ m within the mechanical linewidth, corresponding to the sensitivity 10^{-15} m/$\sqrt{\text{Hz}}$. The zero-point motion of our quartz disk resonators is of the order of $\Delta x_{\text{zp}} \sim 10^{-19}$ m, and hence, it is still beyond the capabilities of our SET-based detectors.

The performance can be improved, first of all, by increasing the sensitivity of the RF-SET to the piezo-charge. In the current setup, the charge sensitivity is around $\sim 10^{-3}$ e/$\sqrt{\text{Hz}}$ that leaves plenty of room for improvement up to the best demonstrated values $\sim 10^{-6}$ e/$\sqrt{\text{Hz}}$ [41]. This entails in particular designing an on-chip tank circuit having a high Q value and also increasing the charging energy by fabricating smaller junctions.

Another limiting factor is that the piezoelectric surface charge originating from the mechanical strain gets spread across a 6-mm-diameter circular area, while our SET-sensitive area, the island, is just 3 µm × 4 µm. This limits the charge coupled to the island to a very small fraction of the total piezoelectric charge generated by a given deformation of the quartz disk. At the moment the amount of charge coupled to the island due to Δx_{zp} is of the order 10^{-8} e. One could increase the island size in order to boost up the coupled charge. However, this would lead to an increase in the island capacitance, decreasing the Coulomb gap and possibly reducing the detector sensitivity. Thus, the island size is a trade-off between the SET sensitivity and the charge it couples to. We note, however, that since quartz has a low dielectric constant $\epsilon_r \sim 4$, the charging energy is currently set by the junctions.

The most important challenge to tackle is to increase the mechanical Q value, allowing to narrow down the detection bandwidth. With high Q values demonstrated by monolithic quartz resonators, combined with the best charge sensitivities mentioned above, and possibly with low-noise Josephson parametric amplifiers to further reduce the detection noise [42], one would reach the level of sensitivity needed to observe vibrations at the single-quantum level with the current amount of coupled charge. Plano-convex cross-section profile [43] of the quartz disks would focus the mode energy in the center, hence mitigating anchor losses that we believe are limiting the losses.

The work paves the way toward studying massive mechanical resonators near the quantum limit of their motion. Monolithic quartz resonators are suitable for this purpose since they are tangible, sturdy, durable and easily manipulated objects in contrast to other micrometer-sized resonators and can have high-quality factors at frequencies of tens of MHz. They can be easily integrated in other devices without the need of advanced fabrication techniques. The millimeter-sized diameter of the disk resonators provides a large sensing area that can be coupled to other macroscopic object to sense mechanical loadings. It can excel at applications that require a simple design that can measure very small strains over a large sensing area.

References

1. J.A. Sidles, J.L. Garbini, K.J. Bruland, D. Rugar, O. Züger, S. Hoen, C.S. Yannoni, Rev. Mod. Phys. **67**, 249 (1995). https://link.aps.org/doi/10.1103/RevModPhys.67.249
2. T.A. Palomaki, J.D. Teufel, R.W. Simmonds, K.W. Lehnert, Science **342**(6159), 710 (2013). https://doi.org/10.1126/science.1244563. http://science.sciencemag.org/content/342/6159/710
3. E.E. Wollman, C.U. Lei, A.J. Weinstein, J. Suh, A. Kronwald, F. Marquardt, A.A. Clerk, K.C. Schwab, Science **349**(6251), 952 (2015). https://doi.org/10.1126/science.aac5138. http://science.sciencemag.org/content/349/6251/952
4. J.M. Pirkkalainen, E. Damskägg, M. Brandt, F. Massel, M.A. Sillanpää, Phys. Rev. Lett. **115**, 243601 (2015). https://link.aps.org/doi/10.1103/PhysRevLett.115.243601
5. F. Lecocq, J.B. Clark, R.W. Simmonds, J. Aumentado, J.D. Teufel, Phys. Rev. X **5**, 041037 (2015). https://link.aps.org/doi/10.1103/PhysRevX.5.041037
6. A.N. Cleland, M.L. Roukes, Appl. Phys. Lett. **69**(18), 2653 (1996). https://doi.org/10.1063/1.117548
7. A. Cleland, M. Roukes, Sens. Actuators A Phys. **72**(3), 256 (1999)
8. P. Mohanty, D.A. Harrington, M.L. Roukes, Physica B Condens. Matter **284-288**, 2143 (2000). http://www.sciencedirect.com/science/article/pii/S092145269902997X
9. T.F. Li, Y.A. Pashkin, O. Astafiev, Y. Nakamura, J.S. Tsai, H. Im, Appl. Phys. Lett. **92**, 043112 (2008)
10. D.W. Carr, S. Evoy, L. Sekaric, H.G. Craighead, J.M. Parpia, Appl. Phys. Lett. **75**(7), 920 (1999). https://doi.org/10.1063/1.124554
11. H. Kim, D.H. Shin, K. McAllister, M. Seo, S. Lee, I.S. Kang, B.H. Park, E.E.B. Campbell, S.W. Lee, ACS Appl. Mater. Interfaces **9**(8), 7282 (2017). https://doi.org/10.1021/acsami.6b16278
12. G.A. Steele, A.K. Hüttel, B. Witkamp, M. Poot, H.B. Meerwaldt, L.P. Kouwenhoven, H.S.J. van der Zant, Science **325**(5944), 1103 (2009). http://science.sciencemag.org/content/325/5944/1103
13. B. Lassagne, Y. Tarakanov, J. Kinaret, D. Garcia-Sanchez, A. Bachtold, Science **325**(5944), 1107 (2009). http://science.sciencemag.org/content/325/5944/1107
14. P.F. Cohadon, A. Heidmann, M. Pinard, Phys. Rev. Lett. **83**, 3174 (1999)
15. S. Gigan, H.R. Böhm, M. Paternostro, F. Blaser, G. Langer, J.B. Hertzberg, K.C. Schwab, D. Bäuerle, M. Aspelmeyer, A. Zeilinger, Nature **444**, 67 (2006)
16. O. Arcizet, P.F. Cohadon, T. Briant, M. Pinard, A. Heidmann, Nature **444**, 71 (2006)
17. C.A. Regal, J.D. Teufel, K.W. Lehnert, Nat. Phys. **4**, 555 (2008)
18. D.J. Flees, J.E. Lukens, Phys. Rev. Lett. **78**, 4817 (1997). https://link.aps.org/doi/10.1103/PhysRevLett.78.4817
19. P. Joyez, P. Lafarge, A. Filipe, D. Esteve, M.H. Devoret, Phys. Rev. Lett. **72**, 2458 (1994). https://link.aps.org/doi/10.1103/PhysRevLett.72.2458
20. R.G. Knobel, A.N. Cleland, Nature **424**(6946), 291 (2003). https://doi.org/10.1038/nature01773
21. M.D. LaHaye, O. Buu, B. Camarota, K.C. Schwab, Science **304**(5667), 74 (2004). https://doi.org/10.1126/science.1094419. http://science.sciencemag.org/content/304/5667/74
22. Y.A. Pashkin, T.F. Li, J.P. Pekola, O. Astafiev, D.A. Knyazev, F. Hoehne, H. Im, Y. Nakamura, J.S. Tsai, Appl. Phys. Lett. **96**(26), 263513 (2010). https://doi.org/10.1063/1.3455880
23. M.D. LaHaye, J. Suh, P.M. Echternach, K.C. Schwab, M.L. Roukes, Nature **459**, 960 (2009)
24. A.D. O'Connell, M. Hofheinz, M. Ansmann, R.C. Bialczak, M. Lenander, E. Lucero, M. Neeley, D. Sank, H. Wang, M. Weides, J. Wenner, J.M. Martinis, A.N. Cleland, Nature **464**, 697 (2010)
25. J.M. Pirkkalainen, S.U. Cho, J. Li, G.S. Paraoanu, P.J. Hakonen, M.A. Sillanpää, Nature **494**, 211 (2013)
26. J.M. Pirkkalainen, S.U. Cho, F. Massel, J. Tuorila, T.T. Heikkila, P.J. Hakonen, M.A. Sillanpää, Nature Commun. **6**, 6981 (2015)
27. M.V. Gustafsson, T. Aref, A.F. Kockum, M.K. Ekström, G. Johansson, P. Delsing, Science **346**, 207 (2014)
28. F. Rouxinol, Y. Hao, F. Brito, A.O. Caldeira, E.K. Irish, M.D. LaHaye, Nanotechnology **27**(36), 364003 (2016). http://stacks.iop.org/0957-4484/27/i=36/a=364003
29. J.T. Santos, J. Li, J. Ilves, C.F. Ockeloen-Korppi, M. Sillanpää, New J. Phys. **19**(10), 103014 (2017). http://stacks.iop.org/1367-2630/19/i=10/a=103014
30. M. Woolley, G. Emzir, G. Milburn, M. Jerger, M. Goryachev, M. Tobar, A. Fedorov, Phys. Rev. B **93**, 224518 (2016)
31. R. Knobel, A.N. Cleland, Appl. Phys. Lett. **81**(12), 2258 (2002). https://doi.org/10.1063/1.1507616
32. J.A. Sidles, Appl. Phys. Lett. **58**(24), 2854 (1991). https://doi.org/10.1063/1.104757

33. J. Pettersson, P. Wahlgren, P. Delsing, D.B. Haviland, T. Claeson, N. Rorsman, H. Zirath, Phys. Rev. B **53**, R13272 (1996). https://link.aps.org/doi/10.1103/PhysRevB.53.R13272

34. E.H. Visscher, J. Lindeman, S.M. Verbrugh, P. Hadley, J.E. Mooij, W. van der Vleuten, Appl. Phys. Lett. **68**(14), 2014 (1996). https://doi.org/10.1063/1.115622

35. R. Knobel, C.S. Yung, A.N. Cleland, Appl. Phys. Lett. **81**(3), 532 (2002). https://doi.org/10.1063/1.1493221

36. M.T. Abuelma'atti, Analog Integr. Circuits Signal Process. **61**(3), 223 (2009). https://doi.org/10.1007/s10470-009-9304-z

37. R.J. Schoelkopf, P. Wahlgren, A.A. Kozhevnikov, P. Delsing, D.E. Prober, Science **280**(5367), 1238 (1998). http://science.sciencemag.org/content/280/5367/1238

38. M.H. Devoret, R.J. Schoelkopf, Nature **406**(6799), 1039 (2000). https://doi.org/10.1038/35023253

39. M. Goryachev, D.L. Creedon, E.N. Ivanov, S. Galliou, R. Bourquin, M.E. Tobar, Appl. Phys. Lett. **100**(24), 243504 (2012)

40. M. Blencowe, M. Wybourne, Appl. Phys. Lett. **77**, 3845 (2000)

41. H. Brenning, S. Kafanov, T. Duty, S. Kubatkin, P. Delsing, J. Appl. Phys. **100**(11), 114321 (2006). http://aip.scitation.org/doi/abs/10.1063/1.2388134

42. C. Macklin, C. Macklin, K. OBrien, D. Hover, M.E. Schwartz, V. Bolkhovsky, X. Zhang, W.D. Oliver, I. Siddiqi, Science **350**, 307 (2015)

43. M. Onoe, in *Proceedings of the 2005 IEEE International Frequency Control Symposium and Exposition, 2005.* (IEEE, 2005), pp. 433–441